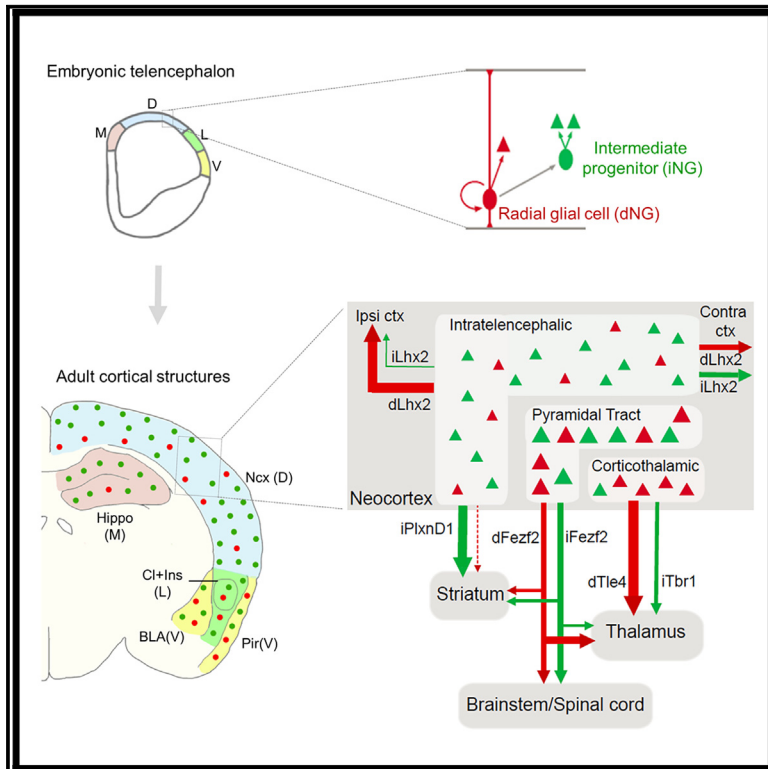


Direct and indirect neurogenesis generate a mosaic of distinct glutamatergic projection neuron types in cerebral cortex

Graphical abstract



Authors

Dhananjay Huilgol, Jesse M. Levine, William Galbavy, Bor-Shuen Wang, Miao He, Shreyas M. Suryanarayana, Z. Josh Huang

Correspondence

josh.huang@duke.edu

In brief

Cortical projection neurons (PNs) are born through direct (dNG) and indirect neurogenesis (iNG). Huilgol et al. establish a genetic strategy to visualize dNG and iNG simultaneously and show their differential contribution to cortical structures. In the neocortex, dNG generates all PN classes; iNG differentially amplifies and diversifies PNs within each class.

Highlights

- Strategy to differentially visualize direct and indirect neurogenesis in the same animal
- dNG and iNG differentially contribute to all cortical structures
- dNG generates all major PN classes; iNG amplifies and diversifies PNs within each class
- dNG and iNG construct distinct cortical projection subnetworks



Article

Direct and indirect neurogenesis generate a mosaic of distinct glutamatergic projection neuron types in cerebral cortex

Dhananjay Huilgol,^{1,3} Jesse M. Levine,^{3,4} William Galbavy,^{3,5} Bor-Shuen Wang,³ Miao He,^{3,6} Shreyas M. Suryanarayana,¹ and Z. Josh Huang^{1,2,3,7,*}

¹Department of Neurobiology, Duke University Medical Center, Durham, NC 27710, USA

²Department of Biomedical Engineering, Duke University, Durham, NC 27708, USA

³Cold Spring Harbor Laboratory, Cold Spring Harbor, NY 11724, USA

⁴Program in Neuroscience and Medical Scientist Training Program, Stony Brook University, Stony Brook, NY 11794, USA

⁵Program in Neuroscience, Department of Neurobiology and Behavior, Stony Brook University, Stony Brook, NY 11794, USA

⁶Institutes of Brain Science, State Key Laboratory of Medical Neurobiology and MOE Frontiers Center for Brain Science, Department of Neurobiology, Zhongshan Hospital, Fudan University, Shanghai 200032, China

⁷Lead contact

*Correspondence: josh.huang@duke.edu

<https://doi.org/10.1016/j.neuron.2023.05.021>

SUMMARY

Variations in size and complexity of the cerebral cortex result from differences in neuron number and composition, rooted in evolutionary changes in direct and indirect neurogenesis (dNG and iNG) that are mediated by radial glia and intermediate progenitors (IPs), respectively. How dNG and iNG differentially contribute to neuronal number, diversity, and connectivity are unknown. Establishing a genetic fate-mapping method to differentially visualize dNG and iNG in mice, we found that while both dNG and iNG contribute to all cortical structures, iNG contributes the largest relative proportions to the hippocampus and neocortex. Within the neocortex, whereas dNG generates all major glutamatergic projection neuron (PN) classes, iNG differentially amplifies and diversifies PNs within each class; the two pathways generate distinct PN types and assemble fine mosaics of lineage-based cortical subnetworks. Our results establish a ground-level lineage framework for understanding cortical development and evolution by linking foundational progenitor types and neurogenic pathways to PN types.

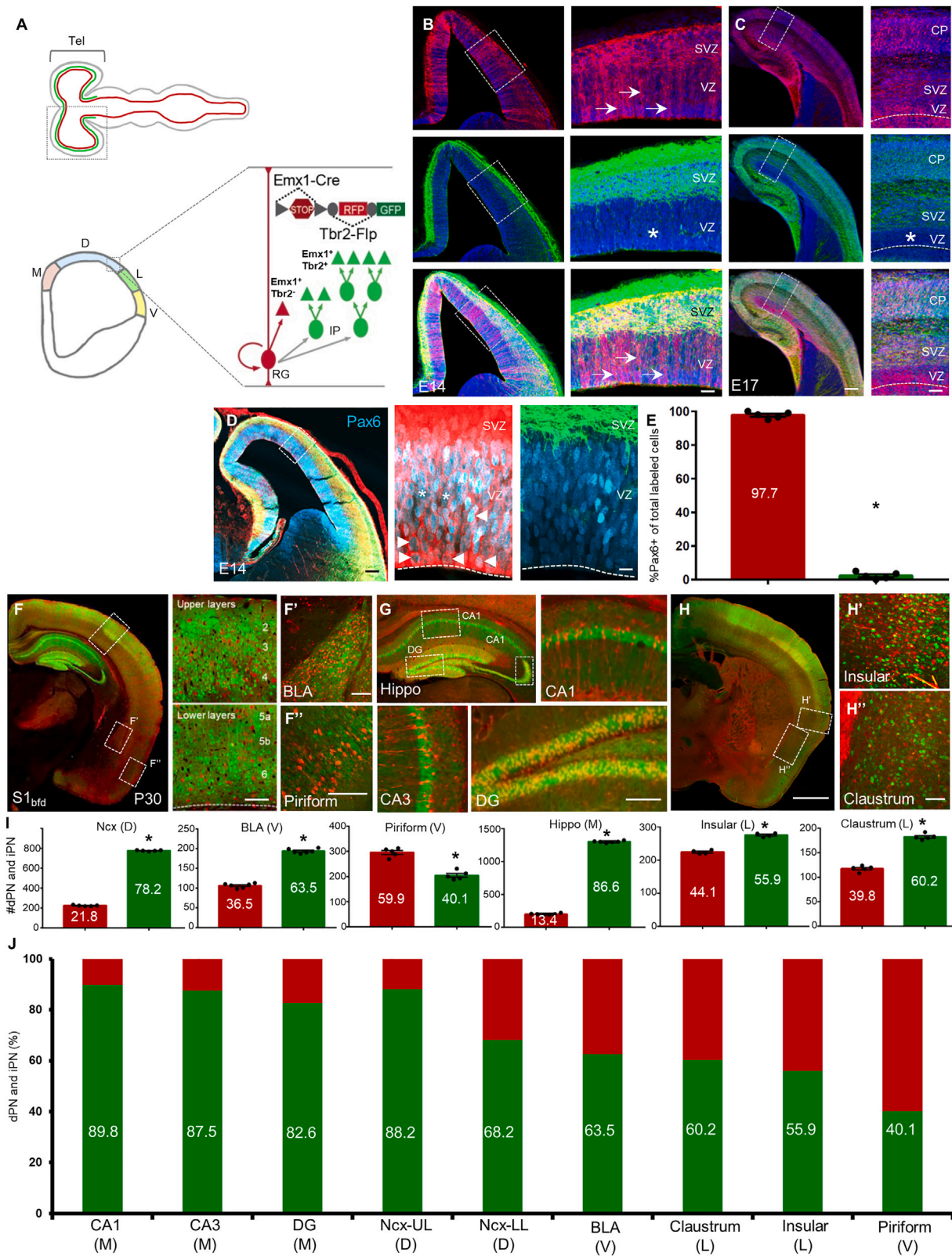
INTRODUCTION

The cerebral cortex is the largest brain structure in mammals comprising vast and diverse nerve cells that enable high-level brain functions, but the developmental mechanisms and logic underlying its neuronal diversity remain poorly understood. Cortical development begins with neurogenesis from progenitors lining the embryonic cerebral ventricle wall, which undergoes two fundamental forms of cell division that give rise to all glutamatergic neurons.¹ In direct neurogenesis (dNG), a radial glial cell (RG) undergoes asymmetric division to self-renew as well as generate one neuronal progeny^{2–5}; in indirect neurogenesis (iNG), RG asymmetric division produces an intermediate progenitor (IP), which then undergoes symmetric division to generate two neurons.^{6–9} Whereas dNG is ubiquitous along the neural tube that gives rise to the central nervous system, iNG is restricted to the telencephalon giving rise to the forebrain, especially the cerebral cortex.⁸ Across evolution, while RG-mediated dNG originated before the dawn of vertebrates and has been conserved ever since, IP-mediated iNG is thought to

have emerged in the last common ancestors (LCAs) of amniotes and subsequently diverged along two different evolutionary paths.¹ Along the sauropsids clade, dNG has dominated neuronal production across different pallial structures, including the 3-layered dorsal cortex of extant non-avian reptiles and the pallia of most avian species; iNG has remained rudimentary in most sauropsids, only to expand in certain birds (corvids) where it drives increased neuron numbers and density in nuclear structures of their pallium.^{10–12} By contrast, along the synapsids path, iNG has expanded tremendously, particularly in the dorsal pallium, and is thought to drive the evolutionary innovation of a six-layered neocortex (Ncx).^{13–16} While the amplification of cortical neuron production through IPs is inherent to iNG,⁶ how dNG and iNG coordinate to generate the increasing diversity of glutamatergic projection neuron (PN) types that assemble cortical networks has remained unknown.

Across the embryonic pallial subdivisions, the medial domain gives rise to the hippocampal formation, the dorsal domain to the Ncx, the lateral domain to the insular cortex (Ins) and claustrum (Cl), and the ventral domain to the piriform cortex (Pir) and





(legend on next page)

the pallial amygdala.¹ Among these, the six-layered Ncx comprises hierarchically organized pyramidal neuron (PyN) classes, each containing multiple finer-grained molecular and projection-defined subtypes.^{17,18} Within this hierarchy, the intratelencephalic (IT) class mediates myriad processing streams within the cerebral hemisphere (including ipsilateral and contralateral intracortical and striatal projections), and the extratelencephalic (ET) class mediates subcortical outputs, including pyramidal tract (PT) neurons that project to all subcortical targets and the corticothalamic (CT) neurons that exclusively target the thalamus.¹⁷ A major unresolved question is how dNG and iNG contribute to the generation of different genetic and projection-defined PyN types—the basic elements of neocortical circuit assembly and function. Furthermore, a quantitative assessment of dNG and iNG contribution to the broadly defined pallial/cortical structures and associated cytoarchitectures have not been achieved. Addressing these questions requires a method to distinguish dNG and iNG and track their developmental trajectories from progenitor types to PN types in the same animal.

Here, we deploy a novel genetic fate-mapping method to simultaneously visualize dNG and iNG as well as their PN progeny in mature cortex in mice. We have previously systematically generated mouse genetic tools targeting RG, IP, and PN types.¹⁹ Here, we establish a genetic intersection-subtraction (IS) strategy and demonstrate that while dNG and iNG generate PNs for all cortical structures, iNG makes increasing contributions to cortical structures along the ventral-dorsal-medial axis, with the largest contributions to the Ncx and hippocampus (Hippo). Within the Ncx, while dNG generates all major IT, PT, and CT classes, iNG differentially amplifies and diversifies PyN types within each class, with disproportionately large contribution to the IT class. Importantly, dNG- and iNG-derived PyN subtypes across as well as within genetically defined major subpopula-

tions show distinct projection patterns, suggesting that they assemble fine mosaics of lineage-specified and evolutionarily rooted cortical subnetworks. Our results reveal a ground-level lineage basis of cortical development and evolution by linking foundational progenitor types and neurogenic mechanisms to PN types and their connectivity.

RESULTS

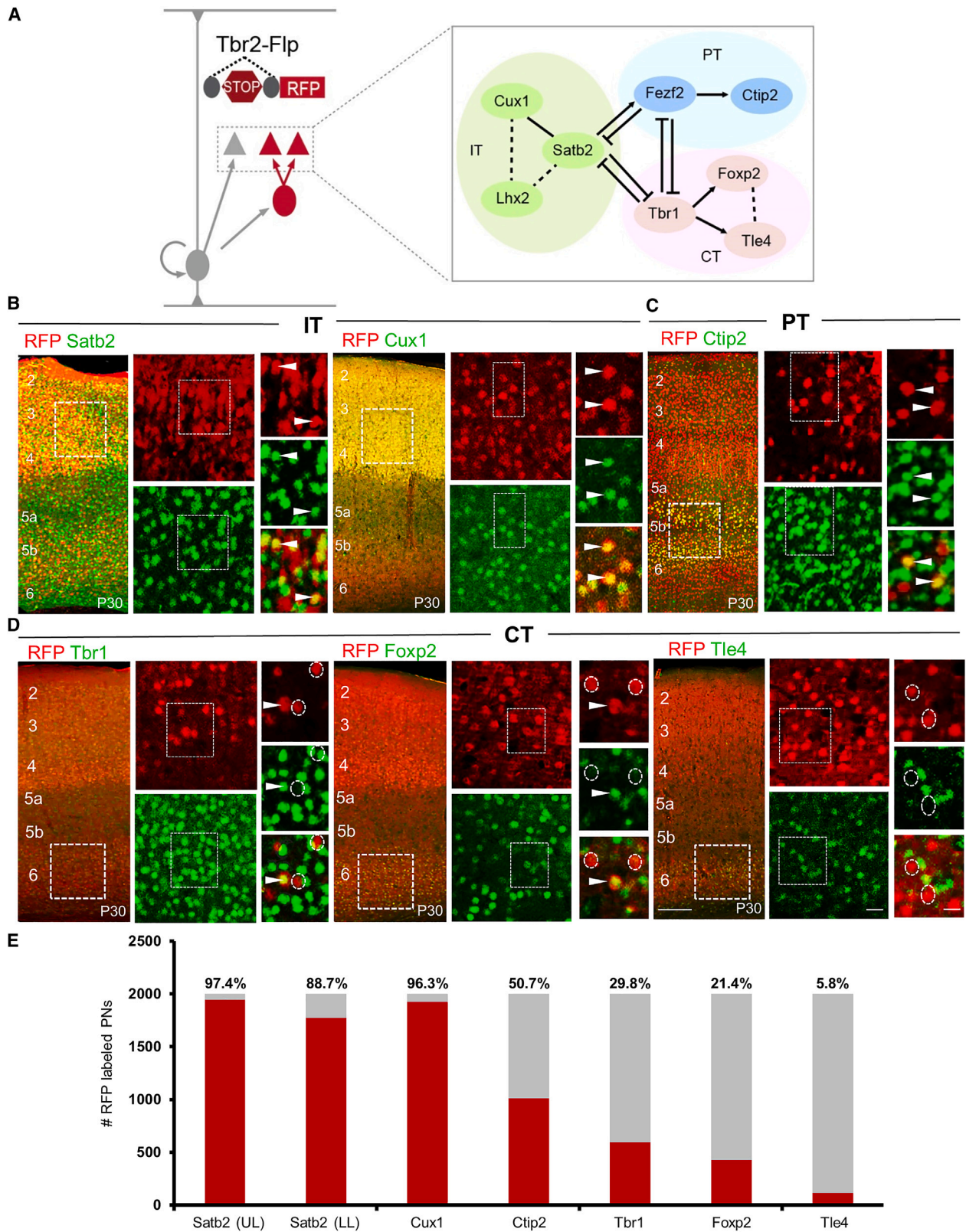
A genetic strategy for differential labeling of dNG and iNG in the same animal

To distinguish and differentially fate map dNG and iNG in the same animal, we designed a genetic intersection-subtraction (IS) strategy in mice (Figure 1A). As all IPs are defined by the expression of the T-box transcription factor (TF) *Tbr2*,²⁰ we generated a *Tbr2-2A-Flp* gene knockin driver line, orthogonal to multiple Cre driver lines that target RGs and PNs.^{19,21} Similar to our *Tbr2-2A-CreER* driver,¹⁹ the *Tbr2-2A-Flp* driver recapitulates the endogenous expression of TBR2 as early as E10.5 (embryonic day 10.5; Figures S1A–S1F) and specifically marked IPs and their PN progeny across all cortical structures (Figures S1G–S1J). Within the Ncx, *Tbr2-2A-Flp* marked PNs across layers, including the IT, PT, and CT classes (Figures S1H–S1J). Thus the *Tbr2-2A-Flp* driver enables combinatorial fate mapping of iNG and dNG with appropriate Cre driver lines and an IS reporter line (Figures S2A–S2C); whereas Cre expression in RGs allows tracking the developmental trajectories of dNG- and iNG-derived PNs (dPNs and iPNs, respectively) (Figure 2B), Cre expression in postmitotic PNs can resolve their dNG or iNG origin (Figure 2C).

We first combined *Tbr2-2A-Flp* with a *Emx1-Cre* driver²² that targeted RGs and a IS reporter, which expressed red fluorescent protein (RFP) in Cre-NOT-Flp cells and GFP in Cre-AND-Flp cells^{19,23} (Figures S2A–S2C). This strategy enabled

Figure 1. dNG and iNG differentially contribute to PNs across cortical structures

- (A) Top schematic shows that whereas RGs (red) exist throughout the neural tube, IPs (green) are present only in the telencephalon. Bottom coronal view from the boxed region of telencephalon shows the four subdivisions of the pallial neuroepithelium along the medio-lateral axis; medial (M), dorsal (D), lateral (L), and ventral (V) pallia, each generating distinct cortical structures. Within the neuroepithelium, RGs mediate direct neurogenesis (red) and through IPs (green), indirect neurogenesis to produce PNs (triangles). dNG and iNG can be simultaneously visualized by a genetic fate-mapping scheme using the IS reporter with *Emx1-Cre* (RG) and *Tbr2-Flp* (IP) drivers: dNG (*Emx1⁺/Tbr2⁻*) is labeled by RFP through “Cre-NOT-Flp” subtraction; iNG (*Emx1⁺/Tbr2⁺*) is labeled by EGFP through “Cre-AND-Flp” intersection.
- (B) Coronal hemi-sections of the pallial neuroepithelium, showing the labeling of RGs (top) and IPs (middle) and merged image (bottom) at E14. On the right are magnified views of boxed regions in left panels. Arrows indicate RGs soma and radial fibers in the VZ; IPs reside in the SVZ and are absent in the VZ (asterisk).
- (C) Coronal hemi-sections at similar levels as in (B), but at E17. Note the appearance of dNG (RFP)- and iNG (GFP)-derived PNs in the cortical plate (CP).
- (D) Coronal hemi-sections similar to (B) showing immunohistochemistry with anti-Pax6 antibodies (cyan). On the right are magnified views of the inset showing labeling of Pax6 with RGs (left) and IPs (right). Arrowheads indicate colocalization of Pax6 and RFP. Asterisks indicate Pax6(+) cells that are not RFP(+).
- (E) Quantification, 97.7% cells of the total number of labeled cells that colabel with anti-Pax6 antibody are RFP(+).
- (F) Coronal section of the cortex shows both dPNs (RFP) and iPNs (GFP) across laminae (upper and lower layers magnified on the right) in the BLA (F') and piriform cortex (F'').
- (G) Coronal view of the hippocampus shows a large contribution from iPNs in different subfields; CA1, CA3, and DG.
- (H) Anterior coronal section shows dPNs and iPNs in the insular cortex (H') and claustrum (H'').
- (I) Quantification of differential contributions of dNG and iNG across distinct pallial structures; y axes are numbers of PNs quantified. Percentage of dPNs and iPNs indicated in the bar graph for respective structures shown in (F)–(H).
- (J) Quantification of differential contributions of dNG and iNG across distinct pallial structures reveals a gradient of iNG contribution from medial to ventral structures; percentage of iPNs are indicated in the bar graph. Note the high contribution of iPNs to the hippocampus and neocortex and their decrease in cortical structures along the medio-ventral axis. A total of 300–1,000 cells were counted in 4–6 mice for each structure. In (B)–(D), the dashed line indicates the ventricle boundary. Mean values are number of cells \pm SEM. For (E), * $p < 0.0001$ (compared with RFP cells); unpaired Student's t test. For (J), Ncx, BLA, Pir, Hippo, Ins, and Cl, * $p < 0.0001$ (compared with dPN); unpaired Student's t test. For (K), all structures, * $p < 0.0001$ (compared with dPN); unpaired Student's t test. Scale bars: 100 μ m in (B)–(D); 20 μ m in insets (B)–(D); 1 mm in (G) and (H); and 100 μ m in (all other scale bars). Abbreviations: tel, telencephalon; RG, radial glial cell; IP, intermediate progenitor; VZ, ventricular zone; SVZ, subventricular zone; S1_{prf}, primary somatosensory barrel field cortex; BLA, basolateral amygdala; Hippo, hippocampus; DG, dentate gyrus; Ncx, neocortex. See also Figures S1–S4.



(legend on next page)

differential labeling of dNG and iNG and their derived PN progeny in the same mouse. At E14, RFP-labeled RGs resided in the ventricular zone (VZ), characterized by their endfeet at the ventricle wall and radial fibers extending to pial surface (Figure 1B). In contrast, GFP-labeled cells were almost exclusively restricted to the subventricular zone (SVZ) with only very sparse labeling in the VZ (Figures 1B, 1C, and S1B–S1E). By E17, in addition to RFP-labeled RGs and GFP-labeled IPs, dNG- and iNG-derived PNs were differentially labeled in the cortical plate (CP; Figure 1C). RG markers, namely, PAX6 (Figures 1D–1F), SOX2, and NESTIN (Figure S3) showed specific colocalization with majority of RFP-labeled cells indicating their RG identity.

dNG and iNG differentially contribute to distinct pallial structures

To fate map dPNs and iPNS, we first quantified the percentage of RFP- and GFP-labeled neurons across multiple cortical regions in P30 (postnatal day 30) mice. This analysis provides the first quantitative assessment of dNG and iNG contributions across cortical structures. Consistent with previous results,²⁴ dPNs and iPNS constituted 21.8% and 78.2%, respectively, in all neurons of the Ncx (Figure 1I). iNG contributed more to the upper layer (UL) PNs (layers 2–4) with 11.8% dPNs and 88.2% iPNS, compared with 31.8% dPNs and 68.2% iPNS in lower layers (LLs) (layers 5–6; Figure 1J). To substantiate this result, we further used the same IS strategy with the *Lhx2-CreER* or *Fezf2-CreER* drive lines by tamoxifen (TM) induction at E12.5, which may label a different set of RGs.¹⁹ We found that 86.7% and 82.8% PNs are produced from iNG in the *Lhx2-CreER* or *Fezf2-CreER* drivers, respectively (Figure S2). Beyond the Ncx, iNG contributed to a significantly and progressively smaller fraction to the basolateral amygdala (BLA), CI, Ins, and Pir (Figures 1F and 1H–1J), consistent with the higher proportion of cycling IPs in the dorsal pallium compared with the lateral and ventral pallia.²⁵ Surprisingly, iNG makes the largest contribution to PNs in the Hippo, with significantly larger fractions than in the Ncx (89.9%, 87.55, and 82.6% in Cornu Ammonis 1 [CA1], Cornu Ammonis 3 [CA3], and dentate gyrus [DG], respectively) (Figures 1G, 1I, and 1J). Therefore, while both dNG and iNG contribute to all cortical structures, iNG makes larger contribution to more recently evolved structures, with disproportionate contribution to the Ncx and Hippo. Notably, iNG contributes to cerebral structures of diverse cytoarchitectures, from six-layered Ncx to folded sheet of Hippo to nuclear structure of amygdala and CI. The fact that the Hippo contains the largest fraction of iNG-derived PNs suggests that increased iNG per

se might not have directly led to the six-layered cytoarchitecture seen in the Ncx.

iNG amplifies and diversifies neocortical PyN types

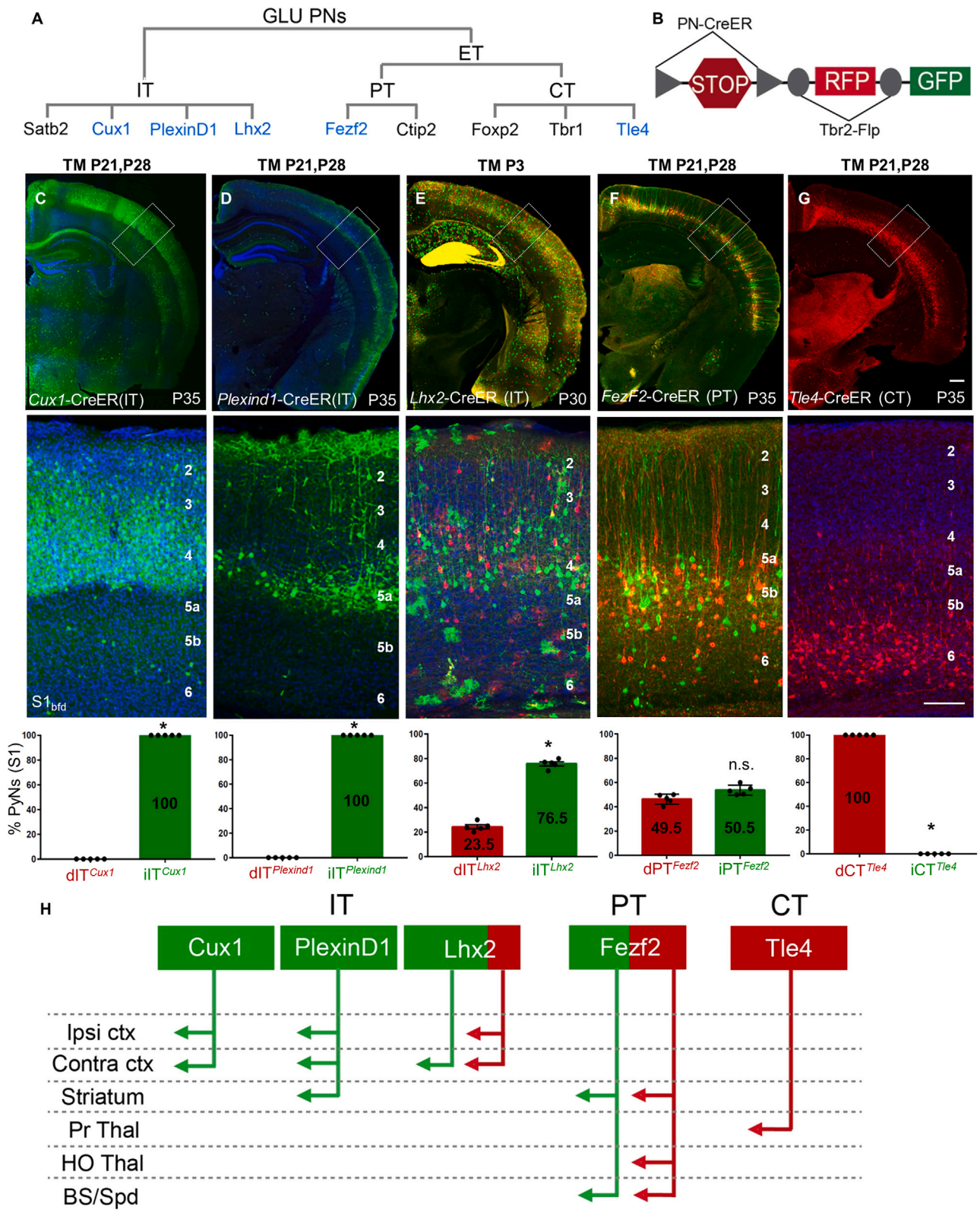
Within the Ncx, dNG and iNG both generated all major projection classes, including IT, PT, and CT (Figure S3). We thus assessed the contribution of iNG to the generation of these major PN classes. Using the *Tbr2-2A-Flp* mice in which all iPNS expressed RFP, we quantified the percentage of RFP cells in a set of lineage-TF-defined PN subpopulations by immunofluorescence (Figure 2A). As expected, the vast majority of SATB2 and CUX1 IT neurons, especially those in ULs, were derived from iNG (Figure 2B). Interestingly, half of the CTIP2-defined PT neurons derived from iNG (Figure 2C). Notably, the large majority (~70%) of CT neurons defined by TBR1 derived from dNG; and within CT neurons, nearly 80% of the FOXP2 subpopulation and the entire TLE4 subpopulation derived from dNG (Figures 2D and 2E). Therefore, although dNG is initiated from the beginning of neurogenesis and generates predominantly deep layer CT and PT neurons, it continues to generate some UL IT neurons during late neurogenesis. Similarly, although iNG is known to generate the vast majority of UL IT neurons during mid-to-late neurogenesis,²⁶ it also makes significant contributions to the early generation of L6 CT and L5 PT neurons.

To substantiate the above result, we deployed our genetic IS strategy, as it can be used to resolve the dNG or iNG origin of mature PN populations (Figure S2C). By combining *Tbr2-Flp* and IS with a set of gene knockin Cre driver lines that define PN subpopulations¹⁹ (Figure 3A), we simultaneously visualized the distribution and morphology of dPNs and iPNS within each subpopulation in the same animal (Figure 3B). Within the IT class, we have previously shown that *Cux1*-positive PNs (PNs^{Cux1}) mainly project within the cortex but not to the striatum, while PNs^{PixnD1} project to ipsilateral and contralateral cortex and striatum.¹⁹ IS labeling by postnatal TM induction in *Cux1-CreER* and *PixnD1-CreER* drivers revealed that all postnatal PNs^{Cux1} and PNs^{PixnD1} were GFP⁺ and thus derived from iNG (Figures 3C and 3D). Interestingly, early postnatal expression of *Lhx2* defines a subset of UL IT PNs,¹⁹ and IS labeling by P3 induction in the *Lhx2-CreER* driver revealed that 23.5% of PNs^{Lhx2} derived from dNG and 76.5% from iNG. dPNs^{Lhx2} and iPNS^{Lhx2} were extensively intermixed across L2/3 (Figure 3E).

Within the PT class, FEZF2 is a master TF that specifies the postmitotic PT fate, and our *Fezf2-CreER* driver captured the large majority of PT PNs.¹⁹ IS labeling by postnatal induction in *Fezf2-CreER* revealed that PNs^{Fezf2} were equally generated

Figure 2. iNG differentially contributes to marker-defined cortical PN classes

(A) Schematic showing a genetic strategy to label all IPs and their derived iPNS using *Tbr2-Flp* and a *Flp*-dependent reporter (also see Figure S1A). Transcriptional network interactions implicated in the postmitotic specification of IT, PT, and CT PNs are also shown. (B) Representative images of immunohistochemistry using antibodies against the TFs in *Tbr2-Flp* brains: anti-SATB2 (left) and anti-CUX1 (right) label IT PNs. (C and D) (C) Anti-CTIP2 labels PT PNs; and (D) anti-TBR1 (left), anti-FOXP2 (middle), and anti-TLE4 (right) label CT PNs. High-magnification views are from insets in low magnification images (left) for each marker. Arrowheads indicate double-positive cells; Dashed circles show non-colocalized RFP⁺ cells. (E) Quantification of immunohistochemical markers that label TF-defined iPNS types in P30 *Tbr2-Flp* mice. Percentages of iPNS positive for a given TF marker are indicated above each bar graph. Quantifications were performed in S1_{brd} from 6 sections (2,000 cells) from 4 to 6 mice each. Mean values are number of marker-positive cells ± SEM. For Satb2, Cux1, Tbr1, Foxp2, and Tle4, *p < 0.0001 (compared with marker-negative RFP cells); unpaired Student's t test. For Ctip2, *p(n.s.) = 0.537 (compared with Ctip2-negative RFP cells); unpaired Student's t test. Scale bars: 100 μm for low-magnification images (left) and 20 μm for high-magnification views (right). Abbreviations: IT, intratelencephalic; PT, pyramidal tract; CT, corticothalamic; UL, upper layer; LL, lower layer; S1_{brd}, primary somatosensory barrel field cortex.



(legend on next page)

from dNG and iNG, and dPNs^{Fezf2} and iPNs^{Fezf2} were extensively intermixed across L5B and L6 (Figure 3F). Finally, the *Tle4-CreER* driver captures a subset of CT PNs, and IS labeling by postnatal induction in *Tle4-CreER* revealed that all PNs^{Tle4} were generated from dNG (Figure 3G). Together, these results demonstrate that dNG and iNG generate distinct subpopulations of PNs within each major class, which project to distinct cortical and subcortical regions (Figure 3H). Compared with primary somatosensory barrel field (S1_{bfd}) (Figure 3), similar proportion and distribution of dPNs and iPNs were observed across different cortical areas including the medial prefrontal cortex (mPFC), primary motor area (M1), and primary visual area (V1) using the constitutive *Emx1-Cre* driver and the *Lhx2-CreER* (IT) and *Fezf2-CreER* (PT) drivers with postnatal TM induction (Figure S4). Therefore, iNG disproportionately diversifies IT over PT and CT subcategories and differentially diversifies genetically defined subpopulations particularly within the IT subclass across the Ncx (Figures 2E and 3H).

Beyond the Ncx, IS labeling also revealed dPNs^{Fezf2} and iPNs^{Fezf2} in the BLA, subiculum, and DG in the Hippo. In addition, dPNs^{Lhx2} and iPNs^{Lhx2} were labeled in the DG in roughly equal ratios, revealing the contribution of iNG to postnatal DG development, as previously shown.²⁷ An equal contribution from dNG and iNG suggests the importance of both neurogenic pathways in creating a mosaic of dentate granule cells (Figure S6). Together, these results suggest the role of both dNG and iNG in the development of PNs^{Fezf2} and PNs^{Lhx2} subpopulations in other cortical structures.

dNG and iNG assemble distinct projection subnetworks

The extensive intermixing of dPN^{Fezf2} with iPN^{Fezf2} and dPN^{Lhx2} with iPN^{Lhx2} further raises the question of whether these lineage-distinct subpopulations represent separate subtypes although they appear similar in laminar position and dendritic morphology. We thus examined whether these subpopulations show differences in their projection patterns. Across their subcortical targets, dPN^{Fezf2} and iPN^{Fezf2} axons remained extensively intermixed, with no clear evidence of targeting distinct regions (Figure S7B). To examine whether dPNs^{Fezf2} and iPNs^{Fezf2} differentially project to specific subcortical targets, we injected a retrograde tracer cholera toxin B subunit (CTB) into several of their targets in postnatal induced *Fezf2-CreER;Tbr2-Flp;IS*

mice (Figures 4A, S7A, and S7B). dPNs^{Fezf2} and iPNs^{Fezf2} in S1_{bfd} projected largely equally to the spinal cord (47.9% and 52.1%, respectively) and striatum (49.1% and 50.9%, respectively) (Figures S7C–S7G). However, of the CTB- and RFP- or GFP-double-labeled PNs, 3 times more dPNs^{Fezf2} (RFP) than iPNs^{Fezf2} (GFP) in S1_{bfd} somatosensory (76.2% and 23.8%, respectively) and caudal forelimb area (CFA) motor cortex (75.4% and 24.6%, respectively) projected to the higher-order thalamic nucleus (posterior, Po nucleus) (Figures 4C–4F).

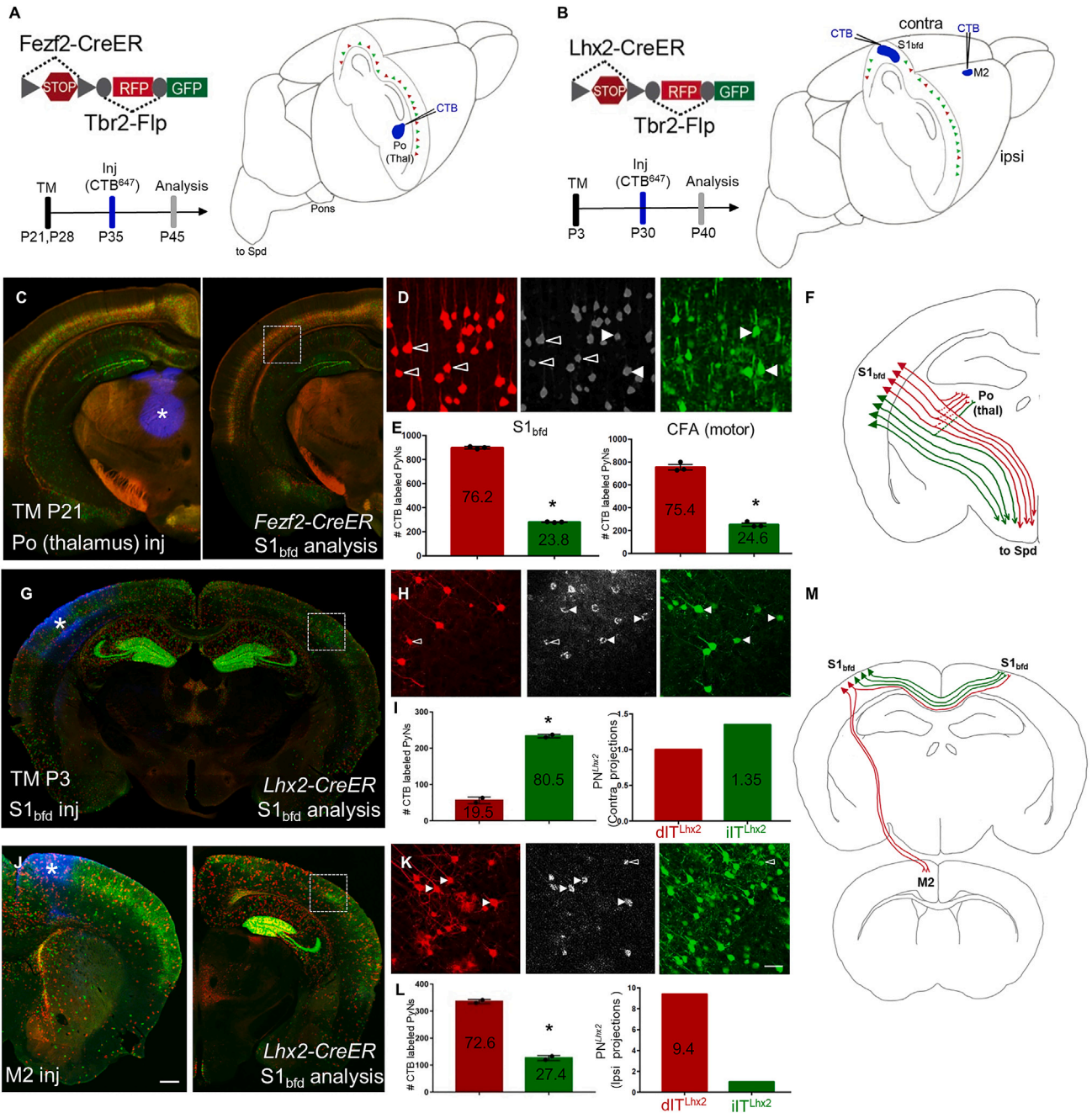
PNs^{Lhx2} projected to the corpus callosum but only sparsely to the striatum (Figures S8B and S8C). To examine potential projection differences between dPNs^{Lhx2} and iPNs^{Lhx2}, we injected CTB in the contralateral S1_{bfd} (contraS1) or ipsilateral M2 (ipsiM2) for analysis in the ipsiS1_{bfd} of P3 induced *Lhx2-CreER;Tbr2-Flp;IS* mice (Figure 4B). The contraS1 received projections from a similar proportion of dPNs^{Lhx2} and iPNs^{Lhx2} in homotypic ipsiS1_{bfd} (Figures 4G–4I), as well as in heterotypic ipsilateral M1, M2, and V1 (Figures S8D–S8G). In sharp contrast, ipsiM2 received a 9.4-fold higher projection from dPNs^{Lhx2} than from iPNs^{Lhx2} in ipsiS1_{bfd} (Figures 4J–4L), and this dPNs^{Lhx2} versus iPNs^{Lhx2} projection difference is 12-fold higher in ipsiM1 and 9.23-fold higher in ipsiS1_{fl} (Figures S8H–S8K). In summary, dPNs^{Lhx2} extend much stronger projections to ipsilateral cortical areas compared with iPNs^{Lhx2}. Therefore, even within the same TF-defined subpopulations that are highly intermixed, dPNs and iPNs show preferential projection patterns (Figures 4F and 4M). Together with the categorical distinction of dNG-generated PNs^{Tle4} and iNG-generated PNs^{Cux1} and PNs^{PlexinD1}, these results indicate that dNG and iNG generate distinct projection subtypes within marker-defined PN subpopulations.

DISCUSSION

Our findings provide the first quantitative assessment of dNG and iNG contributions across cerebral cortical structures and to distinct PN types in the Ncx that assemble different subnetworks. Previous studies have emphasized the role of SVZ/iNG in the generation of UL PNs of the Ncx, suggesting that the rise of iNG in mammals contribute to the formation of a six-layered cytoarchitecture.^{1,13,15,16} Our results demonstrate that iNG in fact contributes to the generation of all pallial/cortical structures in mice, including those which are considered phylogenetically

Figure 3. dNG and iNG differentially contribute to neocortical PN projection types

- (A) GLU PyNs are subdivided into broad IT and ET classes, and ET consists of PT and CT subclasses. Each of these major classes comprises multiple subpopulations defined by marker gene expression. Genes used for generating CreER driver lines are in blue.
- (B) Different *PN-CreER* driver lines, when combined with IS reporter line *Tbr2-Flp*, can simultaneously resolve dNG (Cre-NOT-Flp) and iNG (Cre-AND-Flp) derived subpopulations within a marker gene defined PN type.
- (C and D) (C) PNs^{Cux1} (L2–4 ITs, cortico-cortical PNs) and (D) PNs^{PlexinD1} (subset of L2–5a ITs, cortico-cortical, corticostriatal PNs) were entirely iNG-derived, when corresponding driver lines were induced at P21.
- (E) PNs^{Lhx2} (L2–4 ITs) were predominantly generated from iNG (76.5%) when the corresponding driver line was induced at P3.
- (F) PNs^{Fezf2} (PTs) were generated equally from dNG and iNG when the driver line was induced at P21.
- (G) PNs^{Tle4}, a CT subpopulation, were born entirely from dNG.
- (C–G) Quantifications performed for differential distribution across dNG and iNG (bottom row). Percentage of dPNs and iPNs indicated on the bar graphs.
- (H) dNG (red) and iNG (green) generate distinct genetic- and projection-defined PN subpopulations across IT, PT, and CT classes. Quantifications (C–G, bottom row) were performed in S1_{bfd} from 5 mice for 750–1,500 cells each. Data are mean ± SEM. *p < 0.001 (all) except, p(n.s.) = 0.0204 (PNs^{Fezf2}); unpaired Student's t test. Scale bars, 1 mm (low magnification) and 100 μm (high magnification). Abbreviations: GLU, glutamatergic pyramidal neurons; IT, intratelencephalic; ET, extratelencephalic; PT, pyramidal tract; CT, corticothalamic; S1_{bfd}, primary somatosensory barrel field cortex; Ipsi, ipsilateral; Contra, contralateral; ctx, cortex; Pr Thal, primary thalamus; HO Thal, higher-order thalamus; BS, brainstem; Spd, spinal cord; TM, tamoxifen induction. See also Figures S2 and S4–S6.



(legend continued on next page)

“old” archi- and paleo-cortices. We provide the first quantitative assessment of dNG and iNG contribution across these structures, from the laminated Ncx, Hippo, and Pir to nuclear structures of the amygdala and CI. It is interesting to note that, beyond mammals, the increase of iNG in corvids correlates with the rise of laminated (Wulst/hyperpallium) and nuclear pallial structures (dorsal ventricular ridge, DVR).^{10–12} We further reveal that along the cortical medial-lateral axis, iNG makes progressively lower contributions, with sharp decreases in the amygdala and Pir. Surprisingly, iNG makes the largest relative contribution to the Hippo, significantly greater than its contribution to the Ncx. These results suggest that the rise of iNG per se might not have simply led to the increased lamination in cytoarchitecture (i.e., six-layered Ncx). More likely, the fundamental consequence of iNG is the increase in cell number and diversity, which can assemble multiple forms of cytoarchitectures ranging from a folded cell sheet of the Hippo to six-layered Ncx to nuclear structures such as the amygdala and CI. Consistent with this notion, hippocampal neurogenesis proceeds in parallel with that of the Ncx,^{28–30} and recent single-cell transcriptome analysis in mouse Hippo has revealed a cell type diversity comparable to that of the Ncx.³¹

A key component in neocortical development and evolution has been the diversification of PN types.^{32–35} Although several previous studies showed that iNG generates PNs in all neocortical layers, and particularly those in the ULs,^{26,36,37} and suggested differences in dendritic arborization and electrophysiological properties between *Tbr2*- and non-*Tbr2*-derived PNs within the same cortical layer,^{38,39} these studies have not resolved the relative contributions of dNG and iNG to different PN types. Here, we show that dNG in fact generates all major cortical PyN classes, while iNG differentially amplifies and diversifies PyN types within each class defined by the projection pattern and molecular markers beyond laminar location. iNG not only makes disproportionately large contribution to the IT class as expected, it also contributes to half of the PT class and a significant portion of the CT class. Interestingly, dNG remains the major source of CT class, likely reflecting its dominance over iNG during the early phase of neurogenesis that gives rise to L6 CT neurons. It is conceivable that the CT class may have evolved in mammals from the diversification of ancestral “PT-type” cells, which can be found in several vertebrates.^{40–42}

Furthermore, dPN and iPN types across (PNs^{Cux1}, PNs^{PlexnD1}, and PNs^{Tle4}) as well as within (PNs^{Fezf2}, PNs^{Lhx2}) genetically defined major subpopulations show distinct projection patterns. These results indicate that dNG and iNG assemble a fine mosaic of lineage-based and likely evolutionarily rooted cortical subnetworks (Figure 5). Because RG-dNG and IP-iNG undergo funda-

mentally distinct cell division patterns, their neuronal progenies derive from different birth pattern and order (asymmetric division from RGs versus symmetric cell division from IPs), which likely confer differential chromatin landscapes that impact transcription profiles.⁴⁴ Multi-omics analysis of dPNs and iPNs may reveal their epigenomic and transcriptomic distinctions that underlie their phenotypic distinctions. At the level of circuit connectivity, the categorical distinction between iPNs^{Cux1} and iPNs^{PlexnD1} and dPNs^{Tle4} suggests separate construction of major cortical networks and associated brain systems. Our finding of seemingly more subtle projection differences between dNG- and iNG-derived PN^{Fezf2} and PN^{Lhx2} by retrograde labeling are likely underestimates; methods that quantify synaptic connectivity may reveal further distinction between dPNs and iPNs within genetically defined subpopulations. A major further challenge is to discover whether and how the distinction of dPNs and iPNs manifest at the level of circuit function underlying behavior; such studies require methods to differentially monitor and manipulate the activity of dPNs and iPNs.

Several intracellular and extracellular factors have been shown to influence the balance between dNG and iNG in mammals by affecting the cell division pattern of RGs^{45–48} and intercellular signaling pathways.^{1,49} In particular, the interplay of Robo and Notch signaling levels has been implicated in determining the relative proportion of dNG and iNG across amniotes.¹⁰ High Slit/Robo and low Dll1 signaling are necessary and sufficient to drive dNG, suggesting that modulation in activity levels of conserved signaling pathways is likely a mechanism driving the expansion and increased complexity of the mammalian Ncx during amniote evolution.^{1,10} Comparative studies on the molecular mechanisms of RG division patterns across amniotes will provide further insights into the evolutionary expansion of IPs and iNG.

As brain structures assemble and organize at multiple levels from molecules to cells, embryological territories, and neural circuits, these levels can evolve independently of one another, and homology at one level does not require conservation at other levels. Given that cell types are the elemental units of gene regulation as well as neural circuit assembly, they constitute the basic units of conservation and divergence linking genomic changes to the evolutionary innovations of tissue organization and behavior. Indeed, recent studies suggest that extant amniotes possess a variety of divergent pallial structures, from six-layered Ncx in mammals to three-layered dorsal cortex in non-avian reptiles to nucleus-like pallia in birds. They share a conserved set of neuronal cell types and circuitries, the basic elements of which can be traced back even to the earliest of vertebrates^{1,32,43,50} (Figure 5). A key approach in this cell type perspective of cortical

(K) CTB colocalizes with more dPNs^{Lhx2} (white arrowheads on the left, RFP) compared with iPNs^{Lhx2} (open arrowheads on the right, GFP).

(L) Among CTB- and RFP- or GFP-double-labeled cells in ipsiS1_{bfd}, 72.6% were dPNs^{Lhx2} and 27.4% were iPNs^{Lhx2} (left). When normalized to the ratio of dPNs^{Lhx2} and iPNs^{Lhx2} in ipsiS1_{bfd}, dPNs^{Lhx2} showed a 9.4-fold higher projection to iM2 than iPNs^{Lhx2}.

(M) Summary schematic showing dPNs^{Lhx2} preferentially projecting to ipsilateral cortical areas when compared with iPNs^{Lhx2}. Quantifications were performed in S1_{bfd} or CFA from 1,000 cells, 3–4 mice for PNs^{Fezf2} in (E). Mean values are number of CTB-labeled PNs ± SEM. *p < 0.0001; unpaired Student's t test (compared with dPN); unpaired Student's t test for both S1_{bfd} and CFA. For PNs^{Lhx2}, 300–450 cells were counted from S1_{bfd} in 3–4 animals in (I) and (L). Mean values are number of CTB-labeled PNs ± SEM. *p < 0.0001; unpaired Student's t test (compared with dPN). Scale bars, 1 mm (low magnification; C, G, and J) and 100 μm (high magnification; D, H, and K). Abbreviations: Po, posterior nucleus of thalamus; Thal, thalamus; S1_{bfd}, primary somatosensory barrel field cortex; M2, secondary motor cortex; inj, injection; CFA, caudal forelimb area; Spd, spinal cord; TM, tamoxifen induction. See also Figures S6–S8.

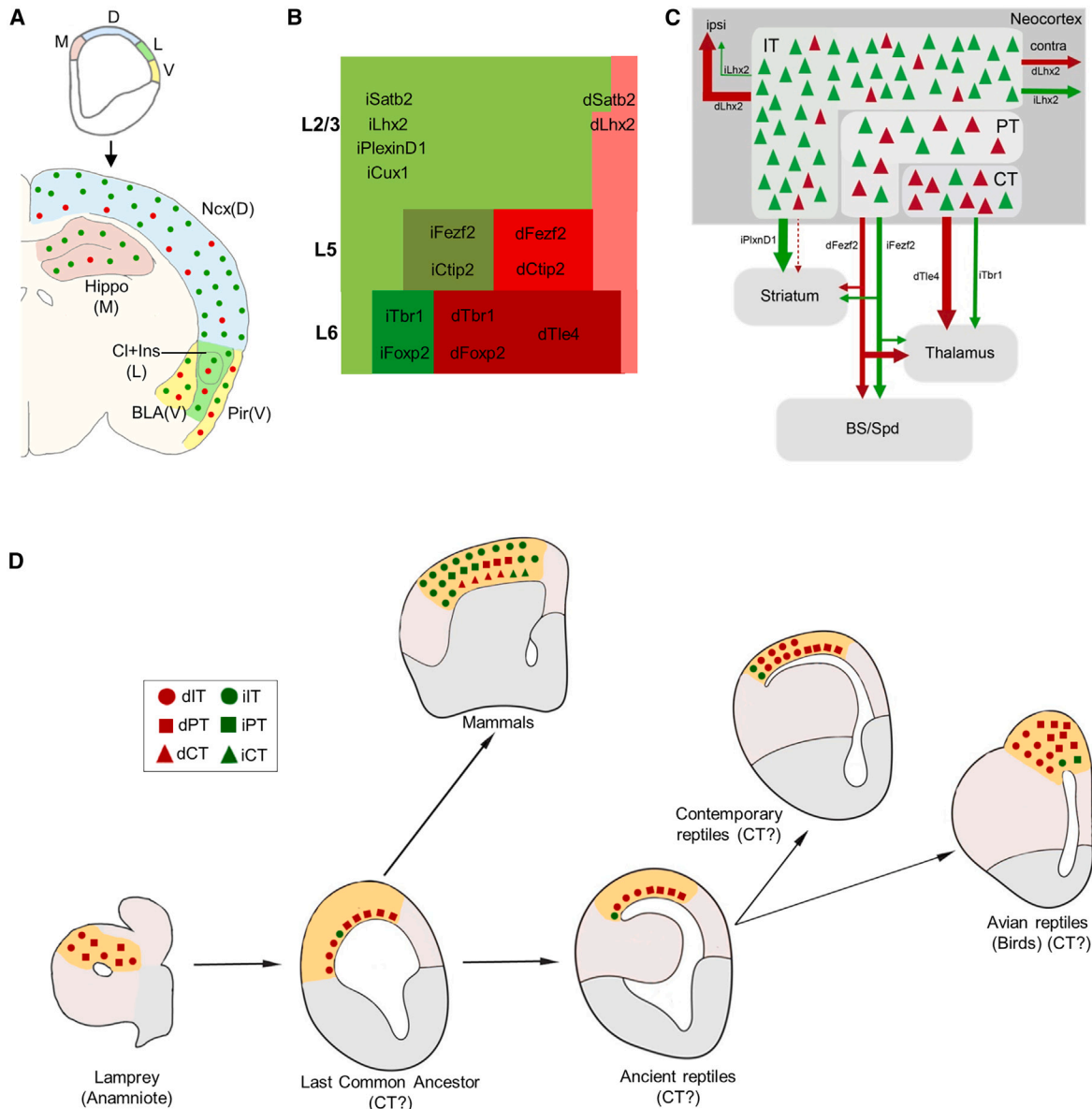


Figure 5. Schematics summarizing dNG and iNG contribution to cortical structures, a mosaic of neocortical PN types and subnetworks, and evolutionary implications

(A) Along the medial to ventral axis of the mouse embryonic pallium, dNG and iNG generate dPNS (red) and iPNS (green) that populate all cortical structures, with decreasing iNG contributions to lateral and ventral structures.

(B) Within the neocortex, dNG generates CT (dark shade), PT (medium shade), and the IT (light shade) class dPNS (red) across layers, whereas iNG differentially amplifies and diversifies genetically defined iPNS types (green) within each class. iPNS have a disproportionately large contribution to the IT class.

(C) dNG (red)- and iNG (green)-derived PN types are highly intermixed within the neocortex, yet show distinct projection patterns both across and within genetically defined subpopulations. Thus, dNG and iNG construct lineage-based fine mosaics of cortical subnetworks.

(D) A conceptual schema depicting the evolutionary trajectory of dNG (red) and iNG (green) with their derived major PN types in dorsal pallial homologs across vertebrates (modified from Suryanarayana et al.⁴³ and Briscoe and Ragsdale³²). dNG and their derived IT (circle) and PT (square) classes are present in lamprey (cyclostomes) and thus predate the dawn of vertebrates. IPs and iNG may have originated in the last common ancestor of amniotes. Among the Sauropsids, dNG has dominated PN production across different pallial structures, including the three-layered dorsal cortex of extant non-avian reptiles and the pallia of most avian species; iNG has remained rudimentary, only to expand in certain birds (corvids) where it drives increased neuron numbers and density in nuclear structures of their pallium. Among Synapsids including mammals, the expansion of iNG greatly amplifies and diversifies PN types across neocortical layers and PN classes. Abbreviations: M, medial pallium; D, dorsal pallium; L, lateral pallium; V, ventral pallium; Ncx, neocortex; Hippo, hippocampus; Cl, claustrum; Ins, insular cortex; BLA, basolateral amygdala; Pir, piriform cortex; ipsi, ipsilateral; contra, contralateral; BS, brain stem; Spd, spinal cord; LCA, last common amniote, IT, intra-telencephalic; PT, pyramidal tract; CT, corticothalamic.

evolution is to delineate the developmental trajectories from progenitor types to neuronal cell types in the assembly of brain circuits. Our finding of distinct developmental trajectories of dNG and iNG begin to provide a ground-level lineage framework of cortical development and evolution by linking foundational progenitor types and neurogenic pathways with conserved and diversified PN types across species, dating from the pan-vertebrate dNG to the emergence of iNG in the amniote LCA.^{1,32,43} Such a cell lineage framework may facilitate exploring the evolutionary origin of the Ncx and its relationship to possible homologous pallial structures across vertebrates.⁴³ Cellular resolution multi-modal analysis based on this lineage framework may guide evolutionary comparisons, linking developmental genetic programs in progenitor types to transcriptome profiles in cell types^{33,34} and to neural circuit organization across cortical structures, including the Ncx.

STAR★METHODS

Detailed methods are provided in the online version of this paper and include the following:

- KEY RESOURCES TABLE
- RESOURCE AVAILABILITY
 - Lead contact
 - Materials availability
 - Data and code availability
- EXPERIMENTAL MODEL AND STUDY PARTICIPANT DETAILS
- METHOD DETAILS
 - Generation of *Tbr2-2A-Flp* knock-in mouse line
 - Generation of Intersection-Subtraction reporter line
 - Tamoxifen induction
 - Immunohistochemistry
 - Primary Antibodies
 - Stereotaxic Injections
 - Imaging
- QUANTIFICATION AND STATISTICAL ANALYSIS

SUPPLEMENTAL INFORMATION

Supplemental information can be found online at <https://doi.org/10.1016/j.neuron.2023.05.021>.

ACKNOWLEDGMENTS

We thank Debra L. Silver, Richard Mooney, and György Buzsáki for comments on the manuscript. We thank L. Li and Priscilla Wu at CSHL for help with the generation of *Tbr2-2A-Flp* knockin, Jonathan Werner for help with quantification related to Figures 2 and 4, the CSHL and Duke University animal resources for mouse husbandry, and the CSHL Microscopy shared resource and Duke University Light Microscopy Core Facility. Funding: NIH grant U19MH114823-01 (Z.J.H.). NIH Director's Pioneer Award 1DP1MH129954-01 (Z.J.H.). Human Frontier Science Program long-term fellowship LT000075/2014-L (D.H.). NARSAD Young Investigator grant no. 26327 (D.H.). NRSA F30 Medical Scientist Predoctoral Fellowship 5F30MH108333 (J.M.L.). NRSA Postdoctoral Fellowship NIH5F32NS096877-03 (B.-S.W.). International Postdoc Grant, Swedish Research Council grant no: 2021-00238 (S.M.S.).

AUTHOR CONTRIBUTIONS

Conceptualization, Z.J.H. and D.H.; experimental design, Z.J.H., D.H., and J.M.L.; experimental investigation, M.H. (design of *Tbr2-2A-FlpO* knockin mouse line), D.H., J.M.L. (fate mapping, immunohistochemistry, imaging, and quantification), D.H., B.-S.W., and W.G. (stereotaxic injections); writing, reviewing, and editing, Z.J.H., D.H., and S.M.S.

DECLARATION OF INTERESTS

The authors declare no competing interests.

INCLUSION AND DIVERSITY

We support inclusive, diverse, and equitable conduct of research.

Received: June 13, 2022

Revised: February 27, 2023

Accepted: May 23, 2023

Published: June 21, 2023

REFERENCES

1. Cárdenas, A., and Borrell, V. (2020). Molecular and cellular evolution of corticogenesis in amniotes. *Cell. Mol. Life Sci.* 77, 1435–1460. <https://doi.org/10.1007/s00018-019-03315-x>.
2. Miyata, T., Kawaguchi, A., Okano, H., and Ogawa, M. (2001). Asymmetric inheritance of radial glial fibers by cortical neurons. *Neuron* 31, 727–741. [https://doi.org/10.1016/s0896-6273\(01\)00420-2](https://doi.org/10.1016/s0896-6273(01)00420-2).
3. Tamamaki, N., Nakamura, K., Okamoto, K., and Kaneko, T. (2001). Radial glia is a progenitor of neocortical neurons in the developing cerebral cortex. *Neurosci. Res.* 41, 51–60. [https://doi.org/10.1016/s0168-0102\(01\)00259-0](https://doi.org/10.1016/s0168-0102(01)00259-0).
4. Noctor, S.C., Flint, A.C., Weissman, T.A., Dammerman, R.S., and Kriegstein, A.R. (2001). Neurons derived from radial glial cells establish radial units in neocortex. *Nature* 409, 714–720. <https://doi.org/10.1038/35055553>.
5. Rakic, P. (2009). Evolution of the neocortex: a perspective from developmental biology. *Nat. Rev. Neurosci.* 10, 724–735. <https://doi.org/10.1038/nrn2719>.
6. Kriegstein, A., Noctor, S., and Martínez-Cerdeño, V. (2006). Patterns of neural stem and progenitor cell division may underlie evolutionary cortical expansion. *Nat. Rev. Neurosci.* 7, 883–890. <https://doi.org/10.1038/nrn2008>.
7. Noctor, S.C., Martínez-Cerdeño, V., Ivic, L., and Kriegstein, A.R. (2004). Cortical neurons arise in symmetric and asymmetric division zones and migrate through specific phases. *Nat. Neurosci.* 7, 136–144. <https://doi.org/10.1038/nn1172>.
8. Haubensak, W., Attardo, A., Denk, W., and Huttner, W.B. (2004). Neurons arise in the basal neuroepithelium of the early mammalian telencephalon: a major site of neurogenesis. *Proc. Natl. Acad. Sci. USA* 101, 3196–3201. <https://doi.org/10.1073/pnas.0308600100>.
9. Miyata, T., Kawaguchi, A., Saito, K., Kawano, M., Muto, T., and Ogawa, M. (2004). Asymmetric production of surface-dividing and non-surface-dividing cortical progenitor cells. *Development* 131, 3133–3145. <https://doi.org/10.1242/dev.01173>.
10. Cárdenas, A., Villalba, A., de Juan Romero, C., Picó, E., Kyriou, C., Tzika, A.C., Tessier-Lavigne, M., Ma, L., Drukker, M., Cappello, S., et al. (2018). Evolution of cortical neurogenesis in amniotes controlled by Robo signaling levels. *Cell* 174, 590–606.e21. <https://doi.org/10.1016/j.cell.2018.06.007>.
11. Nomura, T., Ohtaka-Maruyama, C., Yamashita, W., Wakamatsu, Y., Murakami, Y., Calegari, F., Suzuki, K., Gotoh, H., and Ono, K. (2016). The evolution of basal progenitors in the developing non-mammalian brain. *Development* 143, 66–74. <https://doi.org/10.1242/dev.127100>.

12. Striedter, G.F., and Charvet, C.J. (2009). Telencephalon enlargement by the convergent evolution of expanded subventricular zones. *Biol. Lett.* 5, 134–137. <https://doi.org/10.1098/rsbl.2008.0439>.
13. Cheung, A.F., Kondo, S., Abdel-Mannan, O., Chodroff, R.A., Sirey, T.M., Bluy, L.E., Webber, N., DeProto, J., Karlen, S.J., Krubitzer, L., et al. (2010). The subventricular zone is the developmental milestone of a 6-layered neocortex: comparisons in metatherian and eutherian mammals. *Cereb. Cortex* 20, 1071–1081. <https://doi.org/10.1093/cercor/bhp168>.
14. Florio, M., and Huttner, W.B. (2014). Neural progenitors, neurogenesis and the evolution of the neocortex. *Development* 141, 2182–2194. <https://doi.org/10.1242/dev.090571>.
15. Martínez-Cerdeño, V., Noctor, S.C., and Kriegstein, A.R. (2006). The role of intermediate progenitor cells in the evolutionary expansion of the cerebral cortex. *Cereb. Cortex* 16, i152–i161. <https://doi.org/10.1093/cercor/bhk017>.
16. Villalba, A., Götz, M., and Borrell, V. (2021). The regulation of cortical neurogenesis. *Curr. Top. Dev. Biol.* 142, 1–66. <https://doi.org/10.1016/bs.ctdb.2020.10.003>.
17. Harris, K.D., and Shepherd, G.M. (2015). The neocortical circuit: themes and variations. *Nat. Neurosci.* 18, 170–181. <https://doi.org/10.1038/nn.3917>.
18. Tasic, B., Yao, Z., Graybiuck, L.T., Smith, K.A., Nguyen, T.N., Bertagnolli, D., Goldy, J., Garren, E., Economo, M.N., Viswanathan, S., et al. (2018). Shared and distinct transcriptomic cell types across neocortical areas. *Nature* 563, 72–78. <https://doi.org/10.1038/s41586-018-0654-5>.
19. Matho, K.S., Huilgol, D., Galbavy, W., He, M., Kim, G., An, X., Lu, J., Wu, P., Di Bella, D.J., Shetty, A.S., et al. (2021). Genetic dissection of the glutamatergic neuron system in cerebral cortex. *Nature* 598, 182–187. <https://doi.org/10.1038/s41586-021-03955-9>.
20. Hevner, R.F. (2019). Intermediate progenitors and Tbr2 in cortical development. *J. Anat.* 235, 616–625. <https://doi.org/10.1111/joa.12939>.
21. Franco, S.J., Gil-Sanz, C., Martínez-Garay, I., Espinosa, A., Harkins-Perry, S.R., Ramos, C., and Müller, U. (2012). Fate-restricted neural progenitors in the mammalian cerebral cortex. *Science* 337, 746–749. <https://doi.org/10.1126/science.1223616>.
22. Gorski, J.A., Talley, T., Qiu, M., Puelles, L., Rubenstein, J.L., and Jones, K.R. (2002). Cortical excitatory neurons and glia, but not GABAergic neurons, are produced in the Emx1-expressing lineage. *J. Neurosci.* 22, 6309–6314. <https://doi.org/10.1523/JNEUROSCI.22-15-06309.2002>.
23. He, M., Tucciarone, J., Lee, S., Nigro, M., Kim, Y., Levine, J., Kelly, S., Krugikov, I., Wu, P., Chen, Y., et al. (2016). Strategies and tools for combinatorial targeting of GABAergic neurons in mouse cerebral cortex. *Neuron* 92, 555. <https://doi.org/10.1016/j.neuron.2016.10.009>.
24. Kowalczyk, T., Pontious, A., Englund, C., Daza, R.A., Bedogni, F., Hodge, R., Attardo, A., Bell, C., Huttner, W.B., and Hevner, R.F. (2009). Intermediate neuronal progenitors (basal progenitors) produce pyramidal-projection neurons for all layers of cerebral cortex. *Cereb. Cortex* 19, 2439–2450. <https://doi.org/10.1093/cercor/bhn260>.
25. Moreau, M.X., Saillour, Y., Cwetsch, A.W., Pierani, A., and Causseret, F. (2021). Single-cell transcriptomics of the early developing mouse cerebral cortex disentangle the spatial and temporal components of neuronal fate acquisition. *Development* 148, dev197962. <https://doi.org/10.1242/dev.197962>.
26. Mihalas, A.B., Elsen, G.E., Bedogni, F., Daza, R.A.M., Ramos-Laguna, K.A., Arnold, S.J., and Hevner, R.F. (2016). Intermediate progenitor cohorts differentially generate cortical layers and require Tbr2 for timely acquisition of neuronal subtype identity. *Cell Rep.* 16, 92–105. <https://doi.org/10.1016/j.celrep.2016.05.072>.
27. Hodge, R.D., Garcia, A.J., Elsen, G.E., Nelson, B.R., Mussar, K.E., Reiner, S.L., Ramirez, J.M., and Hevner, R.F. (2013). Tbr2 expression in Cajal-Retzius cells and intermediate neuronal progenitors is required for morphogenesis of the dentate gyrus. *J. Neurosci.* 33, 4165–4180. <https://doi.org/10.1523/JNEUROSCI.4185-12.2013>.
28. Bond, A.M., Berg, D.A., Lee, S., Garcia-Epelboim, A.S., Adusumilli, V.S., Ming, G.L., and Song, H. (2020). Differential timing and coordination of neurogenesis and astrogenesis in developing mouse hippocampal subregions. *Brain Sci.* 10, 909. <https://doi.org/10.3390/brainsci10120909>.
29. Chen, V.S., Morrison, J.P., Southwell, M.F., Foley, J.F., Bolon, B., and Elmore, S.A. (2017). Histology atlas of the developing prenatal and postnatal mouse central nervous system, with emphasis on prenatal days E7.5 to E18.5. *Toxicol. Pathol.* 45, 705–744. <https://doi.org/10.1177/0192623317728134>.
30. Xu, H.T., Han, Z., Gao, P., He, S., Li, Z., Shi, W., Kodish, O., Shao, W., Brown, K.N., Huang, K., et al. (2014). Distinct lineage-dependent structural and functional organization of the hippocampus. *Cell* 157, 1552–1564. <https://doi.org/10.1016/j.cell.2014.03.067>.
31. Yao, Z., van Velthoven, C.T.J., Nguyen, T.N., Goldy, J., Sedeno-Cortes, A.E., Baftizadeh, F., Bertagnolli, D., Casper, T., Chiang, M., Crichton, K., et al. (2021). A taxonomy of transcriptomic cell types across the isocortex and hippocampal formation. *Cell* 184, 3222–3241.e26. <https://doi.org/10.1016/j.cell.2021.04.021>.
32. Briscoe, S.D., and Ragsdale, C.W. (2018). Homology, neocortex, and the evolution of developmental mechanisms. *Science* 362, 190–193. <https://doi.org/10.1126/science.aau3711>.
33. Colquitt, B.M., Merullo, D.P., Konopka, G., Roberts, T.F., and Brainard, M.S. (2021). Cellular transcriptomics reveals evolutionary identities of songbird vocal circuits. *Science* 371, eabd9704. <https://doi.org/10.1126/science.abd9704>.
34. Tosches, M.A., Yamawaki, T.M., Naumann, R.K., Jacobi, A.A., Tushev, G., and Laurent, G. (2018). Evolution of pallium, hippocampus, and cortical cell types revealed by single-cell transcriptomics in reptiles. *Science* 360, 881–888. <https://doi.org/10.1126/science.aar4237>.
35. Arendt, D., Musser, J.M., Baker, C.V.H., Bergman, A., Cepko, C., Erwin, D.H., Pavlicev, M., Schlosser, G., Widder, S., Laubichler, M.D., et al. (2016). The origin and evolution of cell types. *Nat. Rev. Genet.* 17, 744–757. <https://doi.org/10.1038/nrg.2016.127>.
36. Vasistha, N.A., García-Moreno, F., Arora, S., Cheung, A.F., Arnold, S.J., Robertson, E.J., and Molnár, Z. (2015). Cortical and clonal contribution of Tbr2 expressing progenitors in the developing mouse brain. *Cereb. Cortex* 25, 3290–3302. <https://doi.org/10.1093/cercor/bhu125>.
37. Mihalas, A.B., and Hevner, R.F. (2018). Clonal analysis reveals laminar fate multipotency and daughter cell apoptosis of mouse cortical intermediate progenitors. *Development* 145, dev164335. <https://doi.org/10.1242/dev.164335>.
38. Tyler, W.A., Medalla, M., Guillamon-Vivancos, T., Luebke, J.I., and Haydar, T.F. (2015). Neural precursor lineages specify distinct neocortical pyramidal neuron types. *J. Neurosci.* 35, 6142–6152. <https://doi.org/10.1523/JNEUROSCI.0335-15.2015>.
39. Guillamon-Vivancos, T., Tyler, W.A., Medalla, M., Chang, W.W., Okamoto, M., Haydar, T.F., and Luebke, J.I. (2019). Distinct neocortical progenitor lineages fine-tune neuronal diversity in a layer-specific manner. *Cereb. Cortex* 29, 1121–1138. <https://doi.org/10.1093/cercor/bhy019>.
40. Dugas-Ford, J., Rowell, J.J., and Ragsdale, C.W. (2012). Cell-type homologies and the origins of the neocortex. *Proc. Natl. Acad. Sci. USA* 109, 16974–16979. <https://doi.org/10.1073/pnas.1204773109>.
41. Ebbesson, S.O., and Schroeder, D.M. (1971). Connections of the nurse shark's telencephalon. *Science* 173, 254–256. <https://doi.org/10.1126/science.173.3993.254>.
42. Ocaña, F.M., Suryanarayana, S.M., Saitoh, K., Kardamakis, A.A., Capantini, L., Robertson, B., and Grillner, S. (2015). The lamprey pallium provides a blueprint of the mammalian motor projections from cortex. *Curr. Biol.* 25, 413–423. <https://doi.org/10.1016/j.cub.2014.12.013>.

43. Suryanarayana, S.M., Perez-Fernandez, J., Robertson, B., and Grillner, S. (2021). The lamprey forebrain - evolutionary implications. *Brain Behav. Evol.* 96, 318–333. <https://doi.org/10.1159/000517492>.
44. Pinson, A., and Huttner, W.B. (2021). Neocortex expansion in development and evolution—from genes to progenitor cell biology. *Curr. Opin. Cell Biol.* 73, 9–18. <https://doi.org/10.1016/j.ceb.2021.04.008>.
45. Postiglione, M.P., Jüschke, C., Xie, Y., Haas, G.A., Charalambous, C., and Knoblich, J.A. (2011). Mouse *inscuteable* induces apical-basal spindle orientation to facilitate intermediate progenitor generation in the developing neocortex. *Neuron* 72, 269–284. <https://doi.org/10.1016/j.neuron.2011.09.022>.
46. Vitali, I., Fièvre, S., Telley, L., Oberst, P., Bariselli, S., Frangeul, L., Baumann, N., McMahon, J.J., Klingler, E., Bocchi, R., et al. (2018). Progenitor hyperpolarization regulates the sequential generation of neuronal subtypes in the developing neocortex. *Cell* 174, 1264–1276.e15. <https://doi.org/10.1016/j.cell.2018.06.036>.
47. Lv, X., Ren, S.Q., Zhang, X.J., Shen, Z., Ghosh, T., Xianyu, A., Gao, P., Li, Z., Lin, S., Yu, Y., et al. (2019). TBR2 coordinates neurogenesis expansion and precise microcircuit organization via protocadherin 19 in the mammalian cortex. *Nat. Commun.* 10, 3946. <https://doi.org/10.1038/s41467-019-11854-x>.
48. Hasenpusch-Theil, K., Laclef, C., Colligan, M., Fitzgerald, E., Howe, K., Carroll, E., Abrams, S.R., Reiter, J.F., Schneider-Maunoury, S., and Theil, T. (2020). A transient role of the ciliary gene *Inpp5e* in controlling direct versus indirect neurogenesis in cortical development. *eLife* 9, e58162. <https://doi.org/10.7554/eLife.58162>.
49. Taverna, E., Götz, M., and Huttner, W.B. (2014). The cell biology of neurogenesis: toward an understanding of the development and evolution of the neocortex. *Annu. Rev. Cell Dev. Biol.* 30, 465–502. <https://doi.org/10.1146/annurev-cellbio-101011-155801>.
50. Lamanna, F., et al. (2022). Reconstructing the ancestral vertebrate brain using a lamprey neural cell type atlas. <https://doi.org/10.1101/2022.02.28.482278>.

STAR★METHODS

KEY RESOURCES TABLE

REAGENT or RESOURCE	SOURCE	IDENTIFIER
Antibodies		
Rabbit polyclonal Anti-RFP	Rockland	Cat# 600-401-379; RRID:AB_2209751
Chicken polyclonal Anti-GFP	Aves Labs	Cat# GFP-1020; RRID:AB_10000240
Mouse monoclonal Anti-Satb2	Abcam	Cat# ab51502; RRID:AB_882455
Rabbit polyclonal Anti-Cux1	Santa Cruz Biotechnology	Cat# sc-13024; RRID:AB_2261231
Rat monoclonal Anti-Ctip2	Abcam	Cat# ab18465; RRID:AB_2064130
Mouse monoclonal Anti-Foxp2	Santa Cruz Biotechnology	Cat# sc-517261; RRID:AB_2721204
Rabbit polyclonal Anti-Tbr1	MilliporeSigma	Cat# AB10554; RRID:AB_10806888
Mouse monoclonal Anti-Tle4	Santa Cruz Biotechnology	Cat# sc-365406; RRID:AB_10841582
Chicken polyclonal Anti-Tbr2	MilliporeSigma	Cat# AB15894; RRID:AB_10615604
Mouse polyclonal Anti-Pax6	MBL International	Cat# PD022; RRID:AB_1520876
Rabbit polyclonal Anti-Sox2	MilliporeSigma	Cat# AB5603; RRID:AB_2286686
Mouse monoclonal Anti-Nestin	Abcam	Cat# ab22035; RRID:AB_446723
Chemicals, peptides, and recombinant proteins		
Cholera Toxin Subunit B (Recombinant), Alexa Fluor 647	Thermo Fisher Scientific	Cat# C34778
Experimental models: Organisms/strains		
Tbr2-2A-FlpO	This paper	N/A
Emx1-IRES-Cre	JAX; Gorski et al. ²²	RRID:IMSR_JAX:005628
Cux1-2A-CreER	JAX; Matho et al. ¹⁹	RRID:IMSR_JAX:036300
PlexinD1-2A-CreER	JAX; Matho et al. ¹⁹	RRID:IMSR_JAX:036295
Lhx2-2A-CreER	JAX; Matho et al. ¹⁹	RRID:IMSR_JAX:036293
Fezf2-2A-CreER	JAX; Matho et al. ¹⁹	RRID:IMSR_JAX:036296
Tle4-2A-CreER	JAX; Matho et al. ¹⁹	RRID:IMSR_JAX:036298
FSF-tdTomato	Matho et al. ¹⁹	N/A
Intersection-Subtraction (IS)	JAX; He et al. ²² ; Matho et al. ¹⁹	RRID:IMSR_JAX:028582 RRID:IMSR_JAX:036760
Software and algorithms		
Image J	National Institutes of Health	https://imagej.nih.gov/ij/download.html
GraphPad Prism 7	GraphPad	https://www.graphpad.com/features
Excel 2010	Microsoft	https://www.microsoft.com/en-us/microsoft-365/excel
ZEN Software for Image Processing	Zeiss	https://www.zeiss.com/microscopy/en/products/software/zeiss-zen.html

RESOURCE AVAILABILITY

Lead contact

Further information and requests for resources and reagents should be directed to and will be fulfilled by the lead contact, Z. Josh Huang (josh.huang@duke.edu).

Materials availability

Materials generated in this study are available on request to the [lead contact](#). *Tbr2-2A-FlpO* mice generated in this study will be deposited to Jackson Laboratory.

Data and code availability

All data reported in this paper will be shared by the [lead contact](#) upon request.

This paper does not report original code.

Any additional information required to reanalyze the data reported in this paper is available from the [lead contact](#) upon request.

EXPERIMENTAL MODEL AND STUDY PARTICIPANT DETAILS

We have used adult and embryonic genetically targeted mice (*Mus musculus*) in this study. Adult male and female mice have been used in equal or near-equal numbers in all experiments; there are no obvious sex-related differences in the results we report. We have not determined the sex of the animals used for embryonic analysis. All genetically targeted mice have been backcrossed 6 generations to a Swiss-Webster background.

All adult mouse histology experiments were performed on postnatal day (P)28–P35 animals. CTB injections in [Figures 4, S7, and S8](#) were analyzed at P40–P45. We have analyzed embryonic day (E)10.5 embryos for *Tbr2-2A-FlpO* mice, and E14, E17 embryos for *Emx1-IRES-Cre*; *Tbr2-2A-FlpO*; *IS* mice. Developmental and adult ages have been mentioned in Figures, Figure legends and relevant places in the [results](#).

We have used the following knock-in mice in this study: Driver lines include *Tbr2-2A-FlpO*; *Emx1-IRES-Cre* (RRID:IMSR_JAX:005628); *Cux1-2A-CreER* (RRID:IMSR_JAX:036300); *PlexinD1-2A-CreER* (RRID:IMSR_JAX:036295); *Lhx2-2A-CreER* (RRID:IMSR_JAX:036293); *Fzf2-2A-CreER* (RRID:IMSR_JAX:036296) and *Tle4-2A-CreER* (RRID:IMSR_JAX:036298). Reporter lines include *FSF-tdTomato* and *Intersection-Subtraction (IS)* (RRID:IMSR_JAX:028582; RRID:IMSR_JAX:036760).

Mouse related experimental procedures were approved by the Institutional Animal Care and Use Committee (IACUC) of the Cold Spring Harbor Laboratory and Duke University in accordance with NIH guidelines.

METHOD DETAILS

Generation of *Tbr2-2A-Flp* knock-in mouse line

Tbr2-2A-Flp was generated by inserting a 2A-Flp cassette in-frame before the STOP codon of the targeted gene. Targeting vectors were generated using a PCR-based cloning approach as described before.^{19,23}

Generation of Intersection-Subtraction reporter line

The *IS* reporter was generated as described previously^{19,23} (<https://www.jax.org/strain/036760>). Briefly, a STOP cassette flanked with *loxP* sites and dTomato (dimer) sequence flanked with *FRT* sites was targeted at the *Gt(ROSA)26Sor* locus, preventing the transcription of enhanced green fluorescent protein (EGFP). dTomato is expressed following *cre*-mediated recombination, while EGFP is expressed following both *cre*- and *flp*-mediated recombination. The targeting vector was linearized and electroporated into a 129SVj/B6 F1 hybrid ES cell line (V6.5, Open Biosystems). G418-resistant ES clones were first screened by PCR and then confirmed by Southern blotting. Positive ES cell clones were used for tetraploid complementation to obtain heterozygous male mice using standard procedures.

While recombination efficiency of all the *cre*-expressing lines used in this study is ~100%^{19,22} and *Tbr2-Flp* provides near complete recombination, the *IS* reporter requires both *cre* and *flp* recombinations which may not be fully efficient. However, in this study we have assayed the relative proportion of dNG vs iNG and dPN vs iPN, not their absolute numbers. Also, tamoxifen induction of *CreER* recombination will inherently vary, but still report the proportion of dNG vs iNG and dPN vs iPN.

Tamoxifen induction

Tamoxifen (T5648, Sigma) was prepared by dissolving the powder in corn oil (20 mg/ml) and either applying a sonication pulse for 60s or constant magnetic stirring overnight at 37 °C. A 100–200 mg/kg dose was administered by intraperitoneal injection at the appropriate age; If two doses, 100mg/kg doses were administered at P21 and P28. For experiments with *Lhx2-CreER*, 200mg/kg was administered intraperitoneally at P3 from a diluted stock of 5mg/ml.

Immunohistochemistry

Adult mice were anaesthetized (using Avertin) and transcardially perfused with saline followed by 4% paraformaldehyde (PFA) in 0.1 M phosphate buffer. After post-fixation, brains were rinsed three times in PBS and sectioned at a 65–70 μm thickness with a Leica VT1000S vibratome. Embryo heads were collected in PBS and fixed in 4% PFA for 4h at room temperature, rinsed three times with PBS, equilibrated in 30% sucrose-PBS, frozen in OCT compound and cut on a cryostat (Leica, CM3050S) at 25 μm coronal sections. Sections were treated with a blocking solution (10% normal goat serum and 0.2% Triton-X100 in 1X PBS) for 1h, then incubated overnight at 4°C with primary antibodies diluted in the blocking solution. Sections were washed three times in PBS and incubated for 2h at room temperature with corresponding secondary antibodies, Goat or Donkey Alexa Fluor 488, 594 or 647 (1:500, Life Technologies) and DAPI to label nuclei (1:1000 in PBS, Life Technologies, 33342). Sections were washed three times with PBS and dry-mounted on slides using Fluoromount-G (SouthernBiotech, 0100-01) mounting medium.

Primary Antibodies

Anti-GFP (1:1000, Aves, GFP-1020), anti-RFP (1:1000, Rockland Pharmaceuticals, 600-401-379), anti-SATB2 (1:20, Abcam ab51502), anti-CUX1 (1:100, SantaCruz 13024), anti-CTIP2 (1:100, Abcam 18465), anti-TBR1 (1:250, MilliporeSigma AB2261), anti-FOXP2 (1:500, Santa Cruz sc-517261), anti-TLE4 (1:300, Santa Cruz sc-365406), anti-Tbr2 (1:250, EMD Millipore AB15894), anti-Pax6 (1:300, MBL Intnl PD022), anti-Sox2 (1:300, Millipore Sigma AB5603 and anti-Nestin (1:300, Abcam ab22035) were used.

For anti-CTIP2 and anti-SATB2, brains were postfixed in 4% PFA for 4hrs at room temperature. For all other antibodies, postfixation was done overnight at 4°C

Stereotaxic Injections

Adult mice were anaesthetized by 2% isoflurane inhalation with 0.41/min airflow. Preemptive analgesics, 5mg/kg ketoprofen and 0.5mg/kg dexamethasone, were administered subcutaneously before the surgery. Lidocaine (2–4 mg/kg) was applied intra-incisionally. Mice were mounted on a stereotaxic headframe (Kopf Instruments, 940 series), and coordinates were identified. An incision was made over the scalp, a small burr hole drilled in the skull and injections were performed in either the primary somatosensory barrel field cortex ($S1_{\text{bfd}}$): 1.7 posterior relative to bregma, 3.75 lateral, 0.5–0.3 in depth or in the secondary motor cortex (M2): 1.05 anterior relative to bregma, 1.0 lateral, 0.5 in depth.

A pulled glass pipette tip of 20–30 μm containing CTB⁶⁴⁷ (ThermoFischer Scientific, C34778) or AAV (Addgene, AAV-PHP.eB) was lowered into the brain. A 500nl (CTB) or 300–400nl (AAV) volume was delivered at a 30nl/min using a Picospritzer (General Valve Corp); to prevent backflow, the pipette was maintained in place for 10 min prior to retraction. The incision was sutured with Tissueglue (3M Vetbond), following which mice were kept warm at 37°C until complete recovery.

Imaging

All imaging was done using Zeiss LSM 710, 780 or 900 (CSHL St. Giles Advanced Microscopy Center, Duke University Light Microscopy Core Facility and our laboratory) fluorescence confocal microscopes using objectives, 5x for tilescan, 10x or 20x for z-stacks. For embryos, high magnification images were obtained using 63x oil objective. To determine colocalization in adult mouse brains (Figure 2), confocal z-stacks were obtained centered in $S1_{\text{bfd}}$, using a 20x objective. We manually determined colocalization for the desired markers by looking in individual z-planes using ImageJ/FIJI software.

For embryonic experiments (Figures 1, S1, and S3), high-magnification insets are not maximum intensity projections. To observe the morphology of IPs (Figure S1) and quantification of colocalization with RG markers (Figures 1 and S3), only a few sections from the z-plane in low-magnification images have been projected in the high-magnification images. For colocalization experiments with PAX6, SOX2 AND NESTIN in *Emx1-Cre*; *Tbr2-Flp*; *IS* embryonic brains, DAPI was used identify cells since the RFP labeling is across the cell body and along the radial fiber of RGs.

QUANTIFICATION AND STATISTICAL ANALYSIS

All quantifications were performed by two individuals (one blinded). Statistics and plotting of graphs were done using GraphPad Prism 7 and Microsoft Excel 2010.

For embryonic quantifications, we counted 70–200 cells depending on the extent of labeling from at least 5 embryonic brains across 2 litters. For all adult neocortex quantifications, we counted in 1mm x 1mm area from at least 6 sections, from 5–6 adult brains. Number of cells counted for *Emx1-Tbr2-IS* experiment: Neocortex, 1000 cells; CA1, 500 cells; CA3, 500 cells; DG, 500 cells; BLA, 300 cells; Claustrum, 300 cells; Insular cortex, 500 cells; Piriform cortex, 500 cells. For each structure we quantified at least 6 sections from 4–6 brains. To perform molecular characterization of *Tbr2-2A-Flp* brains, we stained vibratome sections for SATB2, CUX1, CTIP2, TBR1, FOXP2 and TLE4. Percentage positive cells were calculated from an average number of 2000 RFP+ cells per staining. Total number of cells counted for *PN-CreER*; *Tbr2-flp*; *IS* experiments for each line was between 750–1500. For *Fezf2-CreER*; *Tbr2-flp*; *IS* and *Lhx2-CreER*; *Tbr2-flp*; *IS* experiments, number of cells counted are: BLA, 300; Subiculum, 500; DG^{Fezf2}, 150; DG^{Lhx2}, 1000. For each driver line we quantified at least 6 sections from 4–6 brains. PN numbers are different due to differences in labelling density.

For CTB quantifications in [Figures 4G–4L](#) and [S6D–S6K](#), “normalization” refers to the ratio of number of CTB/XFP double positive cells to the total number of XFP positive cells observed (XFP is either RFP or GFP). This aided in determine the fold-difference between the projections from dPNs^{Lhx2} and iPNs^{Lhx2} relative to their total number. CTB quantifications for PN^{Fezf2} were done from ~1000 cells from 3-5 mice ([Figures 4](#) and [S5](#)). For PN^{Lhx2}, quantifications were done in ipsiS1_{bfd} from ~300 cells for contraS1_{bfd} and ~450 cells from ipsiM2 injections, from 3-4 brains each ([Figure 4](#)). In [Figure S6](#), from contraS1_{bfd} injections, colocalization was observed in ipsiM1 (~400 cells), ipsiM2 (~90 cells), ipsiV1 (~120 cells). From ipsiM2 injections, colocalization was seen in contraM1 (~200 cells), ipsiM1 (~300 cells) and ipsiS1_{fl} (~500 cells).